ACS APPLIED
NANO MATERIALS

August 7, 2026
Volume 9
Number 31
pubs.acs.org/acsanm

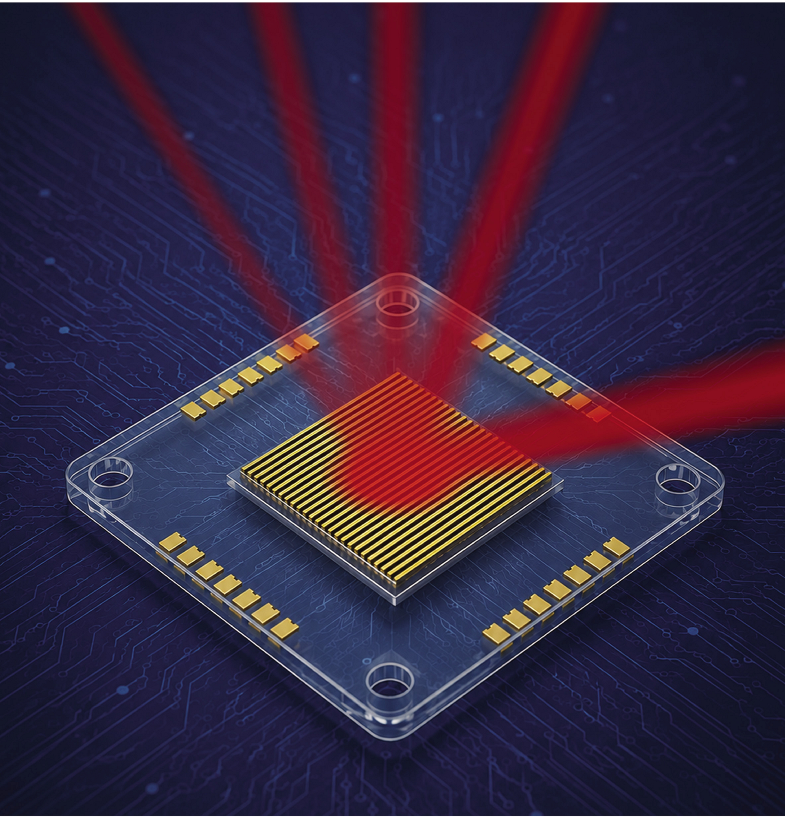

ACS APPLIED NANO MATERIALS

www.acsanm.org

Article

Nanoscale Transmissive Gate-Tunable Conducting Oxide Metagrating for Beam-Steering Modulation

Published as part of ACS Applied Nano Materials special issue "Commemorating the Five-Year Anniversary of the Establishment of NYCU".

Wei-Cheng Tsai, Yi-Hsuan Huang, Yu-Hong Xie, and Yao-Wei Huang*

Cite This: *ACS Appl. Nano Mater.* 2026, 9, 14707−14717

Read Online

ACCESS | Metrics & More | Article Recommendations | Supporting Information

ABSTRACT: We present a nanoscale transmissive gate-tunable conducting-oxide metagrating for beam-steering modulation based on metal−oxide−semiconductor (MOS) field-effect modulation in an indium−zinc oxide (IZO) active layer. The device uses a thin Au/Al_2O_3/IZO/Au nanoscale stack to modulate carrier accumulation and depletion at the oxide interface, enabling voltage-dependent complex transmission near the designed wavelength of 1550 nm. By combining voltage-controlled carrier modulation with a gradient-based inverse-design framework, the proposed platform enables voltage-dependent control of the complex transmission and enhances the simulated diffraction efficiency of the target order. A voltage-dependent meta-atom library is established through electrical and optical simulations and is used to optimize the voltage distribution of multilevel metagratings. Inverse-design optimization predicts that the optimized multilevel voltage distributions achieve relative + first-order diffraction efficiencies of approximately 14% at the designed wavelength of 1550 nm for different deflection angles. As an experimental proof of concept, a forward-designed binary gate-tunable metagrating with a patterned length of 40 μm is fabricated and experimentally characterized at 1564 nm, showing voltage-dependent diffraction and a measured diffraction angle of 51.68°, in close agreement with the theoretical value of 50.81°. These results establish a simulation-guided and experimentally validated foundation for nanoscale conducting-oxide transmissive metagratings and provide a pathway toward future beam-steering and integrated photonic applications.

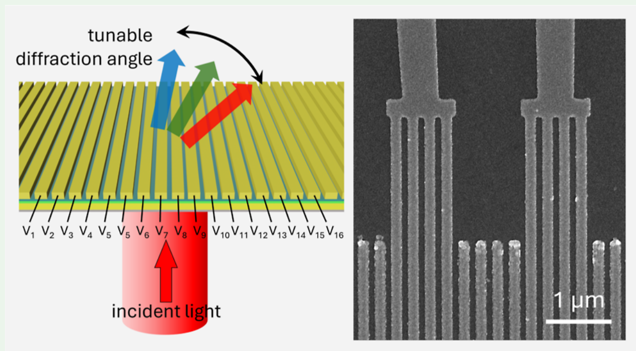

KEYWORDS: *metasurfaces, transparent conducting-oxides, MOS field-effect modulation, inverse design, beam steering, active metasurfaces*

1. INTRODUCTION

Metasurfaces—planar optical components composed of subwavelength nanostructures capable of locally tailoring the phase, amplitude, and polarization of light—have fundamentally reshaped modern optical design. Their ultrathin form factor and precise wavefront control have enabled compact implementations of metalenses,[1,2] beam deflectors,[3] holographic displays,[4−6] and polarization-sensitive elements,[7−10] offering unprecedented levels of integration compared with conventional bulk optics. Despite these advantages, most reported metasurfaces remain intrinsically static: their optical responses are permanently fixed once fabricated. This inherent lack of reconfigurability significantly limits their applicability in advanced optical systems that require dynamic or programmable light manipulation.

To overcome the inherent inflexibility of static devices, considerable efforts have been devoted to developing dynamically tunable metasurfaces.[11,12] Electrically controlled optical elements themselves have a long history: electrically tunable diffraction gratings were demonstrated decades ago using the electro-optic effect in bulk ferroelectric ceramics in a reflective geometry,[13] and voltage-induced refractive-index modulation through the free-carrier plasma-dispersion effect is now routinely used in silicon waveguide phase modulators for optical phased arrays.[14] These established approaches, however, rely on bulk electro-optic media or guided-wave silicon modulation rather than compact, free-space, subwavelength elements. Depending on their mode of operation, tunable platforms can be broadly categorized into reflective,[15−17] and transmissive architectures.[18] Among the various approaches for introducing dynamic reconfigurability—such as

Received: March 30, 2026
Revised: July 9, 2026
Accepted: July 16, 2026
Published: July 22, 2026

thermal tuning,[19] liquid-crystal modulation,[20,21] phase-transition materials,[22] and mechanical modulation,[23,24]—field-effect modulation based on a metal−oxide−semiconductor (MOS) structure directly modulates the carrier concentration in a conducting oxide layer, enabling reversible, spatially localized refractive-index tuning and voltage-controlled optical modulation.[25,26] Previous gate-tunable conducting-oxide metasurfaces have demonstrated modulation speeds exceeding 10 MHz,[15] indicating the potential of MOS field-effect carrier modulation for rapid and reversible optical modulation.

Under an applied gate bias, charge accumulation or depletion at the MOS interface induces voltage-dependent changes in the complex permittivity, thereby enabling simultaneous modulation of the optical amplitude and phase.[15−17] Recent advances have further extended active metasurfaces from purely spatial wavefront control to spatiotemporal modulation, enabling simultaneous control over the spatial and spectral properties of light through combined spatial and temporal tuning.[27] Most electrically tunable metasurfaces demonstrated to date remain predominantly reflective,[15−17,27] which limits their compatibility with compact inline optical systems because of their nonforward-propagating beam paths. In contrast, transmissive metasurfaces are inherently better suited for forward optical architectures and are therefore particularly attractive for applications requiring compact and integrated optical layouts. Nevertheless, existing transmissive tunable designs still involve trade-offs among phase tunability, transmission efficiency, and device complexity, which continue to limit their overall performance.[28]

Recent studies have made important progress in dynamically tunable transmissive metasurfaces using different active material platforms. Gate-tunable transparent conducting oxides, particularly ITO, have been explored for transmissive modulation and phase control through field-effect-induced carrier accumulation, including hybrid plasmonic-waveguide transmission modulators, free-space ITO transmission modulators, and theoretically designed dual-mode ITO metasurfaces with large transmission phase tunability.[29−31] Electro-optic material platforms, such as lithium niobate, organic electro-optic polymers, and silicon−organic hybrid metasurfaces, have further enabled high-speed free-space modulation, guided-mode-resonance-based wavefront shaping, low-voltage operation, and transmissive phase-control schemes.[32−36] Thermo-optic transmissive metasurfaces have also been demonstrated as an alternative route for electrically programmable transmission switching and dynamic beam steering.[37,38] Beyond field-effect conducting oxides and electro-optic or thermo-optic media, silicon free-carrier plasma dispersion has also been numerically employed for transmissive tunable metalenses—for example, by combining a silicon metasurface with a Fabry−Pérot phase shifter to achieve voltage-controlled focus tuning near 1.55 μm.[39] Despite these significant advances, most transmissive tunable metasurfaces have primarily focused on transmission-intensity modulation, resonance tuning, or unit-cell-level phase control. By comparison, voltage-distribution optimization for diffraction-order control in a MOS-based conducting-oxide transmissive metagrating—in particular, an inverse-design framework that tailors the per-element bias for beam steering—remains comparatively unexplored.

In this work, we introduce a nanoscale transmissive gate-tunable conducting-oxide metagrating based on MOS field-effect modulation to address key limitations of existing dynamic metasurface platforms. First, many MOS-based conducting-oxide active metasurfaces have been implemented in reflective configurations, which require folded optical paths and are therefore less compatible with forward-propagating inline optical architectures. Second, transmissive tunable metasurfaces often exhibit limited phase tunability and reduced transmission efficiency, which can significantly constrain diffraction efficiency and beam-steering performance. To overcome these limitations, we combine a transmissive MOS/IZO metagrating architecture with a gradient-based inverse-design framework to optimize diffraction-order control under constrained voltage-dependent amplitude−phase modulation. The device incorporates an interdigitated multi-electrode configuration that enables independent, spatially resolved voltage control across the metasurface, thereby enabling spatially varying control of the complex transmission response. Inverse-design and optimization approaches—including gradient-based optimization,[40−42] topology optimization,[43−46] evolutionary optimization,[47,48] and machine-learning,[49,50]—have been widely applied to metasurface engineering. In particular, inverse-design approaches have also been shown to improve reflective beam-steering performance in active metasurfaces under nonideal phase and amplitude tuning conditions.[51] We employ a gradient-based method to iteratively refine the voltage distribution across the meta-atoms because it is particularly suitable for tunable devices whose optical response varies smoothly with applied voltage. This combination of a compact transmissive architecture, MOS-based carrier-concentration control, and gradient-based inverse design establishes a versatile simulation-guided platform for programmable beam-steering modulation. While LiDAR,[52] dynamic wavefront control, and integrated photonic applications have not been experimentally demonstrated in the present proof-of-concept device, the proposed platform establishes a foundation for these future applications.

2. EXPERIMENTAL SECTION

IZO thin films were deposited by radio frequency (RF) magnetron sputtering and annealed at different temperatures to optimize their electrical and optical properties. To quantitatively model the voltage-dependent optical response of IZO, sputtered films were first characterized using Hall measurements and spectroscopic ellipsometry. These measurements provide baseline electrical and optical parameters, and the complete data set is summarized in Supporting Information S1.

Using the experimentally measured material parameters, the carrier-density distributions under different applied voltages were calculated using a drift-diffusion semiconductor device simulator (Lumerical CHARGE), which solves the coupled Poisson and drift-diffusion equations for the Au/Al_2O_3/IZO/Au MOS stack. The resulting carrier-density distributions are then used to compute the complex permittivity via the Drude model, as described in Supporting Information S2. The voltage-dependent permittivity of IZO is described by

$$\varepsilon_{\mathrm{IZO}}(\omega) = \varepsilon_\infty - \frac{\omega_p^2}{\omega^2 + \mathrm{i}\omega\Gamma} \tag{1}$$

where ε_∞ is the high-frequency permittivity, ω_p is the plasma frequency, and Γ is the damping constant related to the carrier scattering time τ ($\Gamma = 1/\tau$). The plasma frequency is defined as

$$\omega_p = \sqrt{\frac{N_c q^2}{\varepsilon_0 m^* m_e}} \tag{2}$$

https://doi.org/10.1021/acsanm.6c01415
ACS Appl. Nano Mater. 2026, 9, 14707−14717

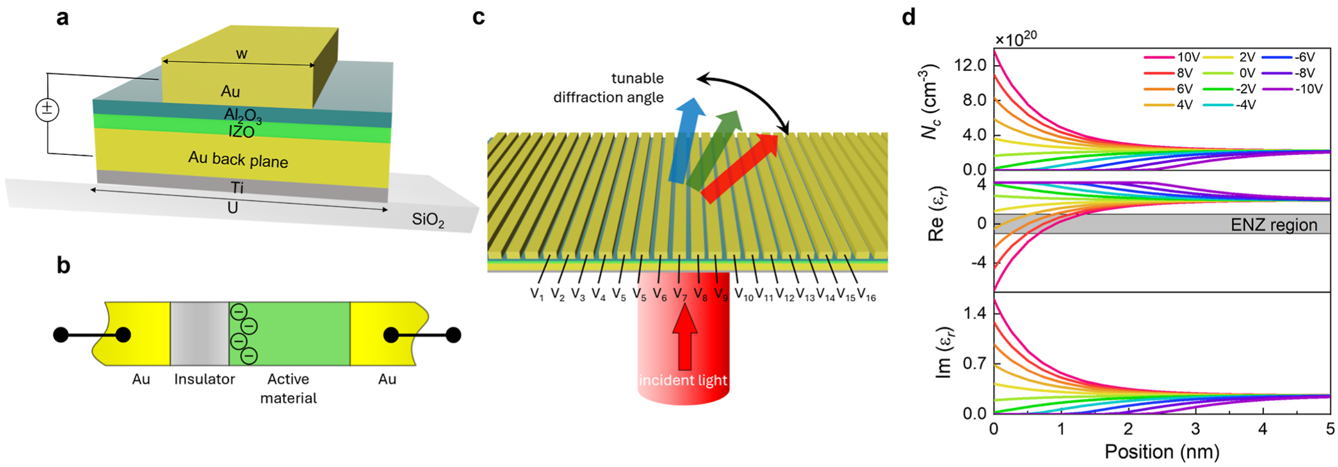

Figure 1. Transmissive gate-tunable metasurface. (a) Schematic of the MOS meta-atom, consisting of a SiO_2 substrate, a Ti adhesion layer, an Au backplane, an IZO active layer, an Al_2O_3 gate dielectric, and a top Au stripe antenna. (b) Schematic illustration of the MOS field-effect mechanism. (c) Conceptual illustration of voltage-controlled beam steering, where different voltages applied to the Au stripes enable tunable diffraction angles and enhanced first-order diffraction efficiency. (d) Simulated depth-dependent profiles of carrier concentration (top), real part of the dielectric permittivity (middle), and imaginary part of the dielectric permittivity (bottom) under different applied voltages.

where N_c is the carrier concentration, q is the elementary charge, ε_0 is the vacuum permittivity, m^* is the effective electron mass, and m_e is the electron rest mass. Variations in the carrier concentration N_c directly modify the plasma frequency and, consequently, the complex permittivity of IZO, enabling voltage-dependent refractive-index tuning. The carrier concentration N_c is determined by both the deposition conditions and the externally applied bias voltage. For the electromagnetic simulations, the Drude parameters of the 300 °C annealed IZO film were $\varepsilon_\infty = 4.3$, $m^* = 0.262$, and $\tau = 5.362$ fs, corresponding to an equilibrium carrier concentration of $N_c = 2.233 \times 10^{20}$ cm^{-3}. Further details of the annealing-dependent IZO parameters and the electrostatic-to-optical conversion procedure are provided in Supporting Information S1 and S2.

The Au films were deposited using electron-beam evaporation. Although the surface roughness was not quantitatively characterized by atomic force microscopy, no evidence of film discontinuity was observed from scanning electron microscopy (SEM) inspection or during optical characterization of the fabricated devices. The IZO films were deposited by RF magnetron sputtering, whereas the Al_2O_3 dielectric layer was deposited by atomic layer deposition. The metasurface patterning is achieved through electron-beam lithography, and the metal interconnects and electrodes were patterned by photolithography.

For optical characterization, a laser diode with a central wavelength of 1564 nm was employed as the light source. The beam was delivered through an optical fiber, collimated, attenuated by a neutral-density filter, and adjusted to TM polarization using linear polarizers. The collimated beam was focused onto the metasurface using an objective lens (NA = 0.42), and the transmitted light was collected by a second objective lens (NA = 0.65) and recorded by an infrared camera. Further details of the optical measurement setup are provided in Supporting Information S3.

3. RESULTS AND DISCUSSION

3.1. Design of Meta-Atom

To realize voltage-controlled modulation of transmitted light, we designed a metal−oxide−semiconductor (MOS) meta-atom that enables field-effect tuning of the optical response. As illustrated in Figure 1a, the meta-atom consists of a SiO_2 substrate, a Ti adhesion layer, an Au backplane, an IZO active layer, an Al_2O_3 gate dielectric, and a top Au stripe antenna. When a bias voltage is applied between the Au stripe antenna and the Au backplane, carrier accumulation is induced at the Al_2O_3/IZO interface, thereby modifying the optical properties of the IZO layer.

The stripe antenna has a width (W) of 170 nm, and the thicknesses of the Au antenna, Al_2O_3, IZO, and Au backplane layers are 15, 5, 5, and 15 nm, respectively. In addition, a 5 nm Ti adhesion layer is inserted beneath the Au backplane to ensure robust adhesion to the substrate. The lateral periodicity (U) of the unit cell is 250 nm. Figure 1a schematically illustrates the MOS meta-atom configuration, including the SiO_2 substrate and the lateral dimensions W and U, while the layer thicknesses are specified in the text.

The voltage-induced carrier redistribution mechanism is depicted in Figure 1b. When a bias is applied between neighboring electrodes, the resulting electric field modifies the carrier density within the IZO layer, forming either accumulation or depletion regions depending on the polarity of the applied voltage. This field-effect behavior alters the local refractive index of IZO and thus provides the fundamental mechanism enabling dynamic amplitude and phase modulation in transmission.

Building upon this mechanism, we implement a multi-electrode transmissive grating as shown in Figure 1c. Each stripe antenna is connected to an independently addressable electrode, allowing spatially varying voltages to be applied across the grating period. This configuration enables programmable phase modulation of the + first-order diffracted beam, forming the basis for electrically reconfigurable transmissive beam steering.

The voltage-dependent carrier-density and permittivity distributions derived from the model described in the Experimental Section are summarized in Figure 1d. Increasing the applied voltage enhances the carrier concentration near the Al_2O_3/IZO interface, which reduces the real part of the permittivity and pushes it toward the epsilon-near-zero (ENZ, $|\varepsilon_r| < 1$) regime. This ENZ-like response strengthens the electric-field confinement at the Al_2O_3/IZO interface. We note that the increased free-carrier concentration under positive bias can also increase the imaginary part of the permittivity and therefore optical absorption. Thus, the positive-bias response involves a trade-off between enhanced field confinement arising from the ENZ-like condition and increased free-carrier

https://doi.org/10.1021/acsanm.6c01415
ACS Appl. Nano Mater. 2026, 9, 14707−14717

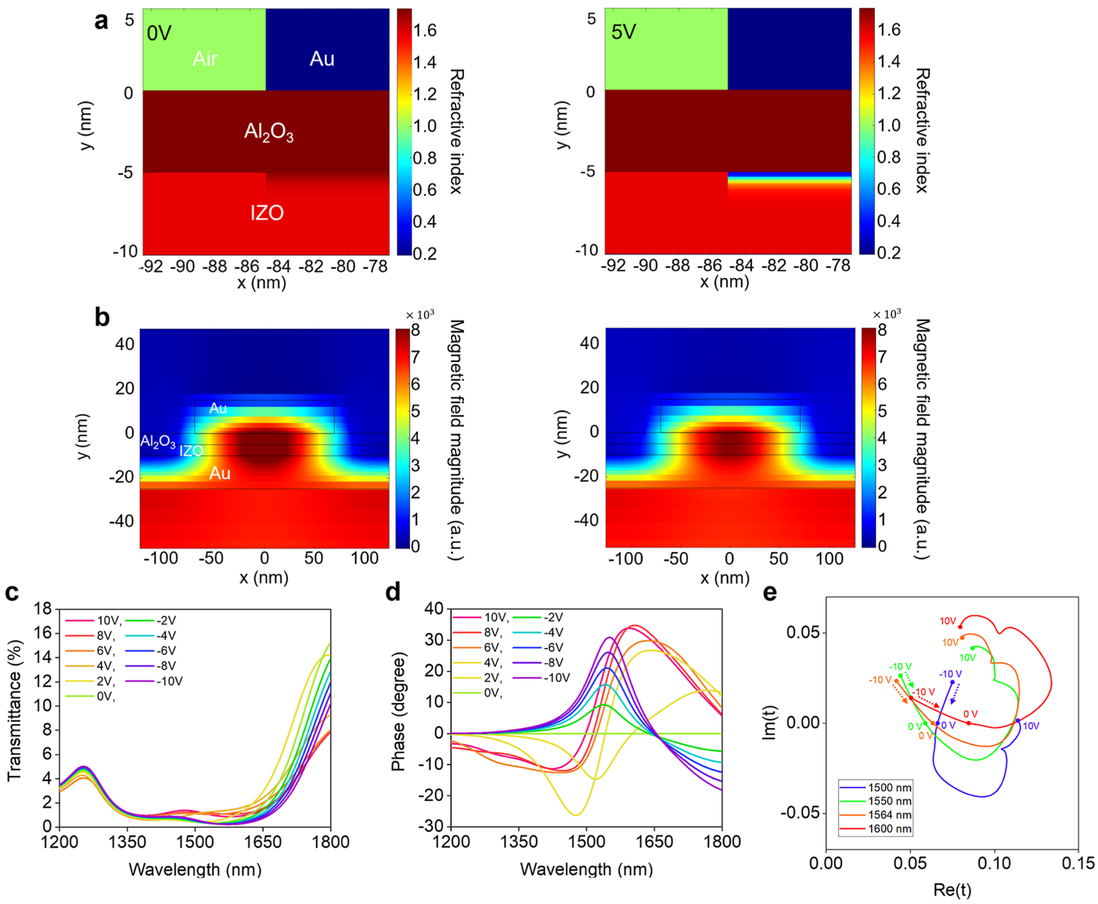

Figure 2. Voltage-dependent optical response of a single meta-atom unit cell obtained using periodic boundary conditions. (a) Refractive-index distributions at 0 V (left) and 5 V (right) at a wavelength of 1550 nm. (b) Simulated magnetic-field distributions at 0 V (left) and 5 V (right), showing the voltage-dependent modulation of the magnetic dipole resonance. (c,d) Simulated transmittance (c) and phase responses (d), respectively, for applied voltages from −10 to 10 V. (e) Complex transmission coefficient in the Re(t)−Im(t) plane at selected wavelengths.

absorption. In the present IZO parameters, however, the imaginary component remains sufficiently moderate to allow voltage-dependent optical modulation. Formally, this field concentration is governed by the continuity of the normal component of the electric displacement field, expressed as

$$\varepsilon_{Al2O3}\mathbf{E}_{Al2O3}\cdot\hat{\mathbf{n}} = \varepsilon_{IZO}\mathbf{E}_{IZO}\cdot\hat{\mathbf{n}} \quad (3)$$

where E_{Al2O3} and E_{IZO} denote the electric fields in insulator (Al_2O_3) and active layer (IZO) respectively, and $\hat{\mathbf{n}}$ represents the normal vector with respect to the surface. When the dielectric permittivity approaches zero, a significant enhancement of the electric field occurs at the interface, thereby increasing the phase modulation capability via field-induced tuning.

Building on the material response shown in Figure 1d, the simulated depth-dependent profiles of carrier concentration and complex dielectric permittivity are plotted as a function of the distance normal to the Al_2O_3/IZO interface. At equilibrium (0 V), a work function difference between the IZO (∼4.49 eV) and the Au backplane (∼5.1 eV) induces band bending, resulting in the formation of a depletion region near the interface. Upon applying a positive bias, an electron accumulation layer emerges at the Al_2O_3/IZO boundary, leading to a pronounced increase in the local carrier concentration. This elevated carrier density drives the real part of the permittivity toward the ENZ region, thereby enabling strong electric-field confinement localized at the interface. In contrast, under a negative bias, although the ENZ-induced field enhancement is absent, the electrically controllable expansion of the depletion region still provides an additional degree of freedom for tailoring the complex amplitude response of the meta-atoms, thereby enabling a broader tunable range of optical modulation. Band-diagram simulations of the Au/Al_2O_3/IZO/Au MOS stack indicate that the negative-bias response within the simulated voltage range is dominated by electron depletion in the highly doped n-type IZO layer, rather than by strong hole inversion. The corresponding band diagrams under positive and negative biases are provided in Supporting Information S2 to further clarify the electrostatic behavior of the IZO layer.

To evaluate how this material modulation affects optical behavior, finite-difference time-domain (FDTD) simulations (Lumerical FDTD) are performed on one meta-atom unit cell with periodic boundary conditions in the lateral direction, representing an infinitely periodic meta-atom array, to quantify its voltage-dependent transmittance and phase. Under TM-polarized incidence, opposite-direction induced charge is excited at the stripe antenna and the Au backplane. The refractive-index profiles at 0 and 5 V are shown in Figure 2a, exhibiting a pronounced change in the index gradient within the active region. The refractive-index profile at 5 V reflects the carrier accumulation-layer formation. The simulated magnetic field distributions at 0 and 5 V, shown in Figure 2b, clearly reveal the voltage-induced modulation of the magnetic dipole

https://doi.org/10.1021/acsanm.6c01415
ACS Appl. Nano Mater. 2026, 9, 14707−14717

resonance, which serves as the primary mechanism governing both the amplitude and phase variations. The operating wavelength can be tailored by adjusting the geometric parameters of the stripe antenna. In our design, targeting an operating wavelength near 1550 nm leads to an optimized antenna width of 170 nm. The voltage-dependent transmittance and phase responses from −10 to 10 V are shown in Figure 2c,d. This voltage range is used as an idealized numerical design space to evaluate the potential field-effect modulation of the MOS/IZO meta-atom, rather than as the experimentally accessible operating range of the fabricated devices. In the present devices, reliable optical measurements could only be performed within a substantially smaller voltage range because increased leakage and device-to-device variability were observed at higher biases. Therefore, the simulated voltage range should be interpreted as a design-space exploration of the potential MOS field-effect modulation rather than a practical operating condition of the fabricated devices. These results indicate that the magnetic dipole resonance provides calculated but limited phase modulation, with a maximum phase change of approximately 30° relative to the 0 V state. Therefore, the present MOS/IZO meta-atom does not provide full (2π) phase coverage and should be regarded as a complex-amplitude modulator rather than a phase-only meta-atom. This limited phase tunability is one of the primary motivations for employing inverse-design-assisted voltage optimization, which seeks to maximize the target diffraction order under constrained amplitude−phase modulation conditions. The achievable diffraction efficiency is further limited by the low transmittance near 1550 nm.

To further illustrate the voltage-dependent optical response, the complex transmission coefficient at selected wavelengths is plotted in the Re(t)−Im(t) plane in Figure 2e. For each wavelength, the trajectory is obtained by sweeping the applied voltage from −10 to 10 V. The resulting trajectories reveal the voltage-dependent evolution of the transmission response in the complex plane.

3.2. Forward Design of Binary Metagrating

Based on the bias-dependent optical response of the individual meta-atoms, we first consider forward-designed binary metagrating as an experimentally implementable proof-of-concept configuration. The binary configuration is selected because it can be realized using the present two-electrode device architecture and provides a simple reference for evaluating voltage-dependent diffraction control in a fabricated MOS/IZO metagrating. A representative voltage configuration of N_{cell} = 8 is shown in Figure 3a, where the first four meta-atoms are biased at 0 V and the remaining four are biased at 5 V, thereby forming a binary voltage distribution. Following the same design principle, binary metagratings with N_{cell} = 8, 10, 12, 14, and 16 were systematically analyzed by finite-difference time-domain (FDTD) simulations performed at the designed operating wavelength of 1550 nm. The corresponding deflection angles, absolute efficiencies, and relative efficiencies obtained from the simulations are summarized in Figure 3b,c, with the labeled values indicating the supercell period Λ (in μm).

In this work, the relative efficiency is defined as the power of the target diffraction order normalized to the optical power transmitted through the substrate, while the absolute efficiency is defined as the power of the target diffraction order normalized to the incident optical power before entering the substrate. The simulated results indicate that, although these binary configurations can generate ±1 diffraction orders at the intended angles, both diffraction efficiencies remain low, with the relative efficiency below 3%. This binary configuration is used to verify the predictable voltage-dependent diffraction response of the MOS/IZO meta-atoms in a realizable device geometry, rather than to represent an optimized blazed metagrating. Because the present MOS/IZO meta-atoms exhibit coupled amplitude and phase modulation rather than pure phase modulation, the binary metagrating serves as a simple proof-of-concept reference rather than the uniquely optimal forward-designed beam-steering configuration. These results show that a simple binary voltage assignment is insufficient to efficiently direct optical power into a single target diffraction order, even though the desired diffraction angles can be generated. This limitation motivates the use of inverse design, in which the voltage applied to each meta-atom is optimized independently to achieve more effective phase−amplitude engineering and higher first-order diffraction efficiency.

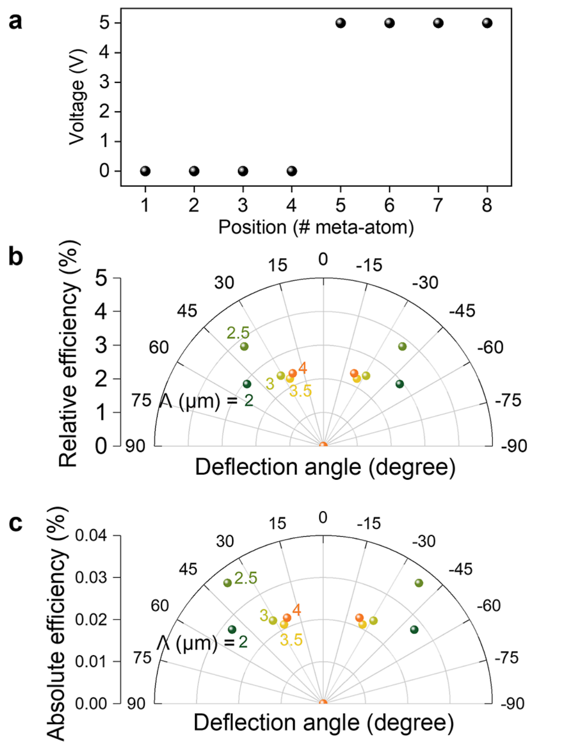

Figure 3. Forward-designed binary metagratings simulated at 1550 nm. (a) Representative binary voltage configuration within one supercell. (b) Simulated deflection angles and relative efficiencies as functions of the supercell period (Λ). (c) Simulated absolute efficiencies as functions of the supercell period (Λ).

3.3. Inverse Design of Metagrating

In our inverse-design framework, the tunable parameter for each meta-atom is its applied bias voltage, and the figure of merit (FOM) is defined as a quantity proportional to the + first-order transmittance. The mathematical definition of the FOM is given

$$\mathrm{FOM} = T_1(\mathbf{V}) \quad (4)$$

where V denotes the voltages assigned to all meta-atoms within one supercell period, and T_1(V) represents the calculated absolute + first-order transmissive diffraction efficiency. The

https://doi.org/10.1021/acsanm.6c01415
ACS Appl. Nano Mater. 2026, 9, 14707−14717

overall optimization workflow is shown in Figure 4a. A voltage-dependent meta-atom library is first constructed using FDTD

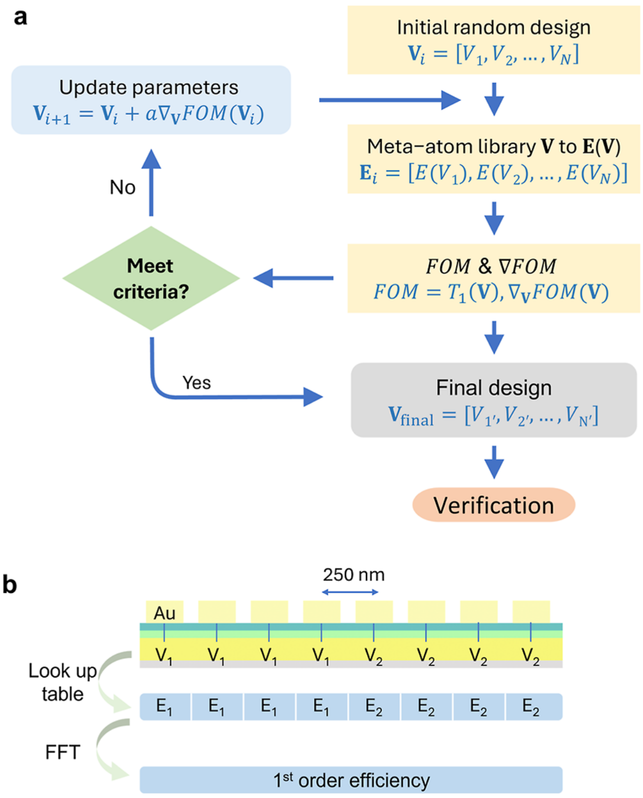

Figure 4. (a) Flowchart of the inverse design optimization process. (b) Schematic illustration of the efficiency calculation using FFT for diffraction-order evaluation at the designed wavelength of 1550 nm.

simulations (Figure 2c-2e), providing the complex transmittance of each meta-atom for voltages between −10 V and +10 V. During optimization, this library enables rapid retrieval of the required complex transmittance values without performing repeated full-wave simulations.

A detailed description of the FFT-based forward model is provided in Supporting Information S4. For any trial voltage configuration, the complex transmittance values of the meta-atoms within one supercell are assembled into a discretized phase−amplitude profile. A Fourier transform is then applied to obtain the far-field diffraction spectrum, from which the + first-order spectral component is used to evaluate T_1. This FFT-based forward model provides the fast evaluations required for iterative optimization, and the full mathematical formulation of T_1 is given in Supporting Information S4. The reliability of the FFT-based evaluation is further examined by comparison with full-wave FDTD results for representative optimized metagratings, as described in Supporting Information S5. We note that this FFT-based forward model is based on a locally periodic, single-meta-atom-library approximation and assumes an infinitely periodic grating; it therefore does not explicitly account for finite-aperture (edge) effects or nonlocal coupling between adjacent, differently biased meta-atoms. Nevertheless, the close agreement between the FFT-based predictions and the corresponding full-wave FDTD simulations indicates that these approximations provide an accurate description for the optimized structures investigated in this work. The final optimized designs are independently cross-checked using full-wave FDTD simulations.

To update the design variables, we compute the gradient of the FOM using a central finite-difference approximation, given as

$$\nabla_{\mathbf{V}}\mathrm{FOM}(\mathbf{V_i}) = \lim_{\Delta V\to 0}\frac{\mathrm{T_1}(\boldsymbol{V} + \Delta V\mathbf{e}_i) - \mathrm{T_1}(\boldsymbol{V} - \Delta V\mathbf{e}_i)}{2\Delta\mathrm{V}} \quad (5)$$

where i denotes the index of the meta-atom being perturbed and e_i is the unit vector corresponding to the ith design variable. At each iteration, a small voltage perturbation ΔV is applied to every single meta-atom, the resulting changes in diffraction efficiency are evaluated using the FFT model, and the voltages are updated along the direction that increases the FOM.

The optimization terminates after a fixed number of iterations. Because gradient-based optimization may converge to local maximum, a multistart strategy is employed in which the optimization is repeatedly initialized from randomized voltage distributions. For each supercell configuration, the optimized solutions with the highest relative efficiency among the multistart trials are retained for further analysis.

Having validated the optimization approach, we next apply it to the design of a transmissive gate-tunable metasurface based on a multilevel grating architecture for beam steering to different angles at the designed wavelength of 1550 nm. In this work, beam steering is achieved by tailoring the effective grating periodicity through the number of meta-atoms within a single supercell. Specifically, N_{cell} = 8, 10, 12, 14, and 16 are considered, resulting in different supercell periods Λ while maintaining the same meta-atom geometry and lattice constant. are considered, resulting in different supercell periods Λwhile maintaining the same meta-atom geometry and lattice constant.

For each supercell configuration illustrated in Figure 5a, the deflection angle of the + first diffraction order can be predicted as

$$\theta = \sin^{-1}\frac{\lambda}{\Lambda} \quad (6)$$

where λ denotes the operating wavelength. As shown in Figure 5b, the optimized designs maintain relative + first-order diffraction efficiencies of approximately 14% over a range of deflection angles, while the undesired − first-order diffraction is substantially suppressed. The corresponding absolute efficiencies also remain nearly unchanged across different supercell configurations. A detailed comparison of the predicted and optimized diffraction angles is provided in Supporting Information S6. We note that these ±5 V and ±10 V voltage libraries represent numerical design-space studies and do not correspond to the experimentally accessible operating range of the present fabricated device.

To further investigate the influence of the available voltage tuning range on the optimization performance, two voltage constraints, ±5 V and ±10 V, are considered. The resulting diffraction efficiencies are compared in Figure 5c. Extending the allowable voltage range from ±5 V to ±10 V leads to a noticeable enhancement in the + first-order diffraction efficiency across all supercell configurations. These results illustrate the performance improvement achievable with an expanded voltage tuning range within the proposed inverse-design framework. Although the experimentally demonstrated

https://doi.org/10.1021/acsanm.6c01415
ACS Appl. Nano Mater. 2026, 9, 14707−14717

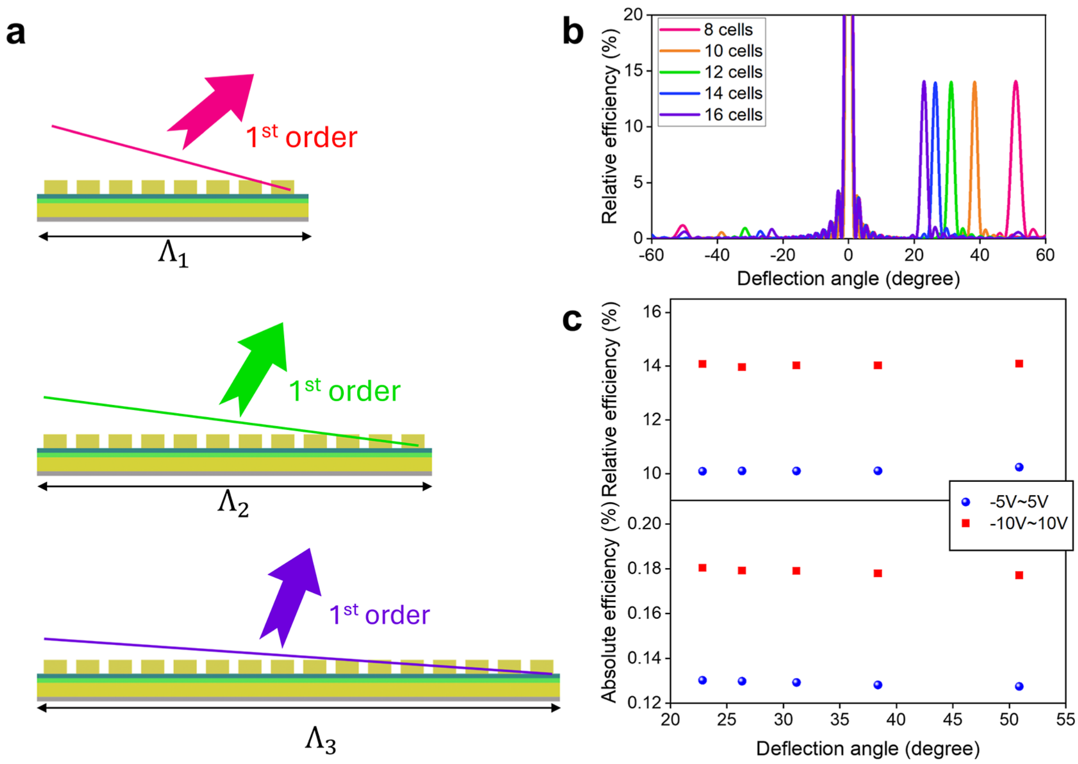

Figure 5. (a) Schematic illustration of multilevel metagratings with different supercell periods Λ for steering the + first-order diffracted beam to different angles. Simulations were conducted at the designed operating wavelength of 1550 nm for meta-atom arrays with N_{cell} = 8, 12, 16, where adjacent meta-atoms are spaced 250 nm apart. (b) FFT-calculated relative efficiency as a function of deflection angle for metagratings with different N_{cell}. (c) Comparison of the relative and absolute diffraction efficiencies obtained using inverse design with voltage libraries spanning ±5 V and ±10 V.

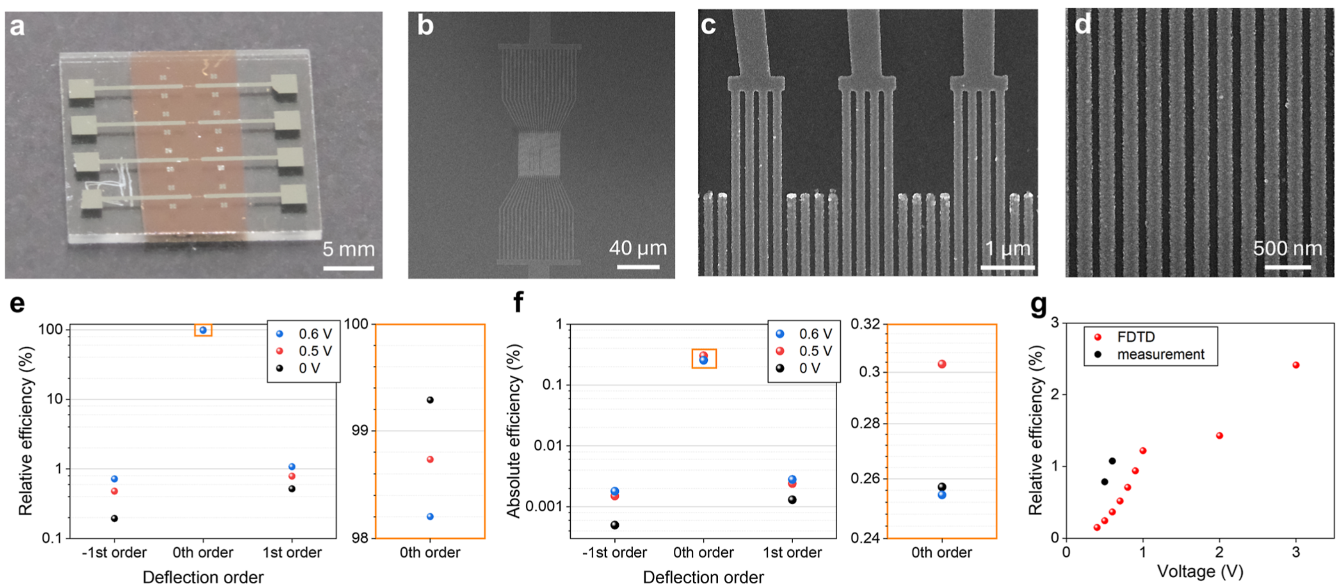

Figure 6. Experimental demonstration of the forward-designed binary gate-tunable metasurface. (a) Optical image of the fabricated sample. (b−d) SEM images of the fabricated metasurface at different magnifications. (e−f) Measured relative and absolute diffraction efficiencies of the − first, 0th, and + first diffraction orders under applied voltages of 0, 0.5, and 0.6 V. Insets in (e) and (f) show enlarged views of the 0th-order region for improved visibility of the measured data points. (g) Comparison of the measured relative + first-order diffraction efficiency with the FDTD results simulated at the experimental wavelength of 1564 nm as a function of the applied voltage.

device operates over a substantially smaller voltage range, the comparison provides useful insight into the potential performance gains that could be realized through future improvements in device engineering and dielectric reliability.

Despite the performance improvement obtained with a wider voltage tuning range, practical material constraints must be carefully considered. Previous MOS-based conducting-oxide metasurfaces employing ultrathin Al_2O_3 or hafnium/aluminum oxide nanolaminate (HAOL) gate dielectrics have

https://doi.org/10.1021/acsanm.6c01415
ACS Appl. Nano Mater. 2026, 9, 14707−14717

reported dielectric breakdown occurring in the few-volt range, corresponding to breakdown fields on the order of several MV/cm, although the exact value depends strongly on dielectric quality, defect density, local thickness variation, electrode morphology, and device area.[15,17] Consequently, the voltage range employed in practical operation is inherently restricted, necessitating a trade-off between diffraction efficiency enhancement and long-term device reliability. Therefore, the extended voltage ranges (e.g., ±5 V and ±10 V) considered in this work should be interpreted as idealized numerical design spaces for evaluating the potential performance of the MOS/IZO platform, rather than as practical operating conditions of the present fabricated devices.

3.4. Experimental Validation of the Gate-Tunable Binary Metagrating

To experimentally validate the proposed voltage-controlled transmissive diffraction mechanism, a forward-designed binary metagrating was fabricated as a proof-of-concept device. Figure 6a shows a photograph of the fabricated device, while the corresponding SEM images are presented in Figure 6b−d. The designed grating line width is 170 nm, whereas the measured line widths are 172 nm at the center and 168 nm at the edge of the device. This close agreement confirms that the fabricated structure closely follows the designed geometry.

The meta-atom and metagrating were designed for an operating wavelength of 1550 nm, whereas the experimental characterization was performed using an available 1564 nm telecom-band laser source. To enable a direct comparison with the experimental results, additional FDTD simulations were carried out at 1564 nm using the measured device geometry. A bias voltage of 0.5 V was initially selected to ensure stable device operation while producing a clearly measurable diffracted spot. The diffraction angle was then determined from the measured displacement of the diffracted spot, yielding a value of 51.68°. This value is close to the theoretical diffraction angle of 50.81° for the N_{cell} = 8 design.

Because beam steering arises from the combined voltage-dependent complex transmission response (i.e., simultaneous amplitude and phase modulation) of the meta-atoms, the redistribution of the transmitted diffraction orders serves as a direct experimental validation of the intended device functionality. Accordingly, the voltage-dependent redistribution of the transmitted diffraction orders is adopted—rather than a direct interferometric phase measurement—as the primary experimental observable.

Figure 6e,f show the measured diffraction efficiencies under different applied voltages. The corresponding measured optical powers and the calculated absolute and relative diffraction efficiencies are summarized in Supporting Information S3. Because the measured zeroth-order relative efficiencies remain close to 98−99% over the investigated voltage range, the corresponding data points nearly overlap near the top of the plots. Enlarged insets are therefore included to improve the visibility of the zeroth-order diffraction data. At 0 V bias, a small but nonzero diffraction efficiency is still observed, which is attributed primarily to weak infrared scattering from the illuminated sample, resulting in a residual signal detected by the power meter. As the bias voltage is increased to 0.5 and 0.6 V, the diffraction efficiency increases accordingly, with the + first-order diffraction efficiency exceeding the − first-order diffraction efficiency at 0.6 V. Specifically, the measured relative + first-order diffraction efficiency increases from 0.7869% at 0.5 V to 1.0768% at 0.6 V, corresponding to an enhancement factor of approximately 1.37. Figure 6g compares the measured relative efficiency with the FDTD results. The experimental results exhibit higher diffraction efficiency than the simulated results. Note that for the fabricated N_{cell} = 8 binary metagrating (supercell period $\Lambda = 2\ \mu$m, $\lambda/\Lambda \approx 0.78$), only the zeroth and ± first diffraction orders are propagating at the operating wavelength, while all higher orders are evanescent. Accordingly, no additional propagating diffraction orders are omitted from the normalization used in either the simulations or the experiments. The experimental and simulated relative efficiencies in Figure 6g are therefore evaluated over the same set of diffraction orders and share an identical normalization. The remaining difference between the measured and simulated results is attributed primarily to the spectral redshift observed in Figure 2c, which increases the transmittance at the experimental laser wavelength of 1564 nm and is therefore expected to increase the measured relative diffraction efficiency.

The results presented above show that the proposed MOS-based conducting-oxide metagrating provides voltage-dependent transmissive diffraction, while also revealing the efficiency limitation of simple binary voltage assignment. The forward-designed binary metagratings generate the designed diffraction angles, but their simulated relative diffraction efficiencies remain below 3%. These results indicate that a binary voltage distribution cannot efficiently concentrate the transmitted optical power into the desired + first diffraction order. In contrast, the inverse-designed multilevel voltage distributions increase the simulated relative + first-order diffraction efficiency to approximately 14% for different supercell configurations, demonstrating that independently optimized voltage distributions can better utilize the available amplitude and phase modulation of the tunable meta-atoms.

The present experimental demonstration confirms voltage-dependent transmissive diffraction in the fabricated forward-designed binary metagrating, whereas the inverse-designed multilevel metagratings are numerically demonstrated in this work. This distinction is important because the optimized efficiencies represent the simulated potential of the proposed voltage-optimization framework, while the fabricated binary device serves as a proof-of-concept verification of the gate-tunable diffraction mechanism. Experimental realization of the inverse-designed beam-steering performance will require the implementation of independently addressable multilevel electrodes together with the associated metal interconnects and voltage-addressing circuitry.

As discussed in Section 3.3, the ±5 V and ±10 V voltage libraries should be regarded as numerical design-space studies rather than experimentally accessible operating conditions. In the present experiment, the applied voltage was conservatively limited to 0.6 V because increased leakage and dielectric failure were observed at higher biases, indicating that practical operation is currently constrained by the reliability of the ultrathin Al_2O_3 gate dielectric. Although increasing the dielectric thickness or improving dielectric quality could increase the voltage tolerance, a thicker dielectric would reduce the gate capacitance and weaken the field-effect-induced carrier accumulation in the IZO layer, thereby reducing the achievable optical modulation depth. Consequently, the proposed platform currently involves a trade-off between optical modulation efficiency and reliable low-voltage operation, highlighting the need for improved materials and multielectrode device implementation.

The inverse-designed metagratings presented in this work are based on periodic supercell architectures, in which the voltage distribution within each supercell is optimized to enhance the + first-order diffraction efficiency. This periodic-supercell strategy provides a direct and physically interpretable relationship between the supercell period and the beam-deflection angle and enables rapid iterative optimization using an FFT-based diffraction model. More general strategies, such as nonperiodic voltage profiles or disorder-assisted amplitude—phase optimization, may provide additional degrees of freedom for further improving diffraction efficiency and suppressing parasitic diffraction orders.[47] However, such approaches would substantially increase the complexity of the design space, device layout, voltage addressing, and experimental implementation, and would likely require more computationally intensive optimization or full-wave validation. Therefore, the periodic supercell-based inverse-design framework adopted here represents a practical balance between optimization flexibility, physical interpretability, and experimental feasibility. Future work will explore the extension of this framework to nonperiodic or disorder-assisted voltage distributions for higher-efficiency transmissive gate-tunable metagratings.

4. CONCLUSIONS

In summary, we have demonstrated a nanoscale transmissive gate-tunable conducting-oxide metagrating based on MOS field-effect modulation in an IZO active layer. By combining voltage-controlled carrier modulation with a gradient-based inverse-design framework, the simulated multilevel voltage distributions achieve substantially improved + first-order diffraction efficiency relative to the simple binary proof-of-concept configuration discussed above. The inverse-designed metagratings are not constrained to binary voltage states; instead, they utilize the full set of available voltage-dependent complex transmission states in the meta-atom library. This comparison is intended to illustrate the potential benefit of exploiting the available bias-dependent complex transmission states through inverse design, rather than to benchmark against an optimized conventional blazed metagrating. For different supercell configurations, the optimized designs reach relative + first-order diffraction efficiencies of about 14%, with corresponding FDTD-verified values close to 10%, highlighting the effectiveness of inverse design for exploring future multilevel transmissive beam-steering applications.

As an experimental proof of concept, we fabricated a forward-designed binary gate-tunable metasurface and experimentally verified voltage-dependent diffraction. The measured diffraction angle of 51.68° is in good agreement with the theoretical value of 50.81° for the N_{cell} = 8 design, and the measured diffraction efficiency increases with applied bias, confirming the feasibility of electrical modulation in the proposed transmissive architecture. Although the present experimental demonstration focuses on a forward-designed binary proof-of-concept device and is currently constrained by the dielectric reliability of the ultrathin Al_2O_3 gate layer, these results establish a practical foundation for future nanoscale conducting-oxide metasurfaces with independently addressable electrodes for dynamic multiangle beam steering. With further improvements in dielectric quality, multielectrode voltage-addressing circuitry, and meta-atom design, the proposed platform could be extended toward higher-efficiency programmable transmissive metasurfaces and may ultimately enable future beam steering, LiDAR, and integrated photonic applications.

■ ASSOCIATED CONTENT

Supporting Information

The Supporting Information is available free of charge at https://pubs.acs.org/doi/10.1021/acsanm.6c01415.

Additional dielectric and electrical properties of annealed IZO films, electrostatic modeling, Drude conversion of voltage-dependent IZO permittivity, optical measurement setup, measured diffraction efficiency, FFT-based evaluation of the FOM, validation of the FFT-based forward model, and diffraction angles and efficiencies for different supercell configurations (PDF)

■ AUTHOR INFORMATION

Corresponding Author

Yao-Wei Huang − *Department of Photonics, College of Electrical and Computer Engineering, National Yang Ming Chiao Tung University, Hsinchu 300093, Taiwan;* orcid.org/0000-0001-8983-413X; Email: ywh@nycu.edu.tw

Authors

Wei-Cheng Tsai − *Department of Photonics, College of Electrical and Computer Engineering, National Yang Ming Chiao Tung University, Hsinchu 300093, Taiwan*

Yi-Hsuan Huang − *Department of Photonics, College of Electrical and Computer Engineering, National Yang Ming Chiao Tung University, Hsinchu 300093, Taiwan*

Yu-Hong Xie − *Department of Photonics, College of Electrical and Computer Engineering, National Yang Ming Chiao Tung University, Hsinchu 300093, Taiwan*

Complete contact information is available at: https://pubs.acs.org/10.1021/acsanm.6c01415

Author Contributions

Y.-W.H. initiated the study and contributed required materials and analysis tools. Y.-H.H. performed numerical calculation and inverse design. Y.-H.H. and Y.-H.X. fabricated metasurface samples and performed measurements. Y.-H.H., W.-C.T., and Y.-W.H. analyzed numerical and experimental data. W.-C.T., and Y.-W.H. wrote the manuscript. All authors discussed the results and commented on the manuscript.

Notes

The authors declare no competing financial interest.

■ ACKNOWLEDGMENTS

This work was supported by the National Science and Technology Council in Taiwan (Grant Nos. 113-2112-M-A49-025 and 114-2112 M-A49-007) and the Ministry of Education in Taiwan under the Yushan Young Fellow Program (Grant Nos. MOE-109-YSFEE-0010-004-P1 and MOE-114-YSFEE-0010-006-P2). The authors acknowledge Dr. Ruzan Sokhoyan, Dr. Yu-Heng Hong, and Dr. Hao-Chung Kuo for the technical discussion. The work was performed in part at the Nano Facility Center (NFC) and the Center for Nano Science and Technology (CNST) in NYCU, Taiwan Semi-

https://doi.org/10.1021/acsanm.6c01415
ACS Appl. Nano Mater. 2026, 9, 14707−14717

conductor Research Institute (TSRI), and Tze-Chiang Foundation of Science & Technology (TCFST).

■ REFERENCES

(1) Hu, Z.; Gu, M.; Tian, Y.; Li, C.; Zhu, M.; Zhou, H.; Fang, B.; Hong, Z.; Jing, X. Review for Optical Metalens Based on Metasurfaces: Fabrication and Applications. *Microsyst. Nanoeng.* **2025**, *11* (1), 189.

(2) Lee, J.-H.; Wang, H.-Y.; Ho, P. Y.; Chung, Y. C.; Duh, R.-T.; Chiang, C.-C.; Horng, R.-H.; Huang, Y.-W.; Tseng, M. L. Water-Immersed GaP Huygens' Meta-Optics for Visible Structured Light Generation. *Adv. Sci.* **2025**, *12* (34), No. e10467.

(3) Yu, N.; Genevet, P.; Kats, M. A.; Aieta, F.; Tetienne, J.-P.; Capasso, F.; Gaburro, Z. Light Propagation with Phase Discontinuities: Generalized Laws of Reflection and Refraction. *Science* **2011**, *334* (6054), 333−337.

(4) Zheng, G.; Mühlenbernd, H.; Kenney, M.; Li, G.; Zentgraf, T.; Zhang, S. Metasurface Holograms Reaching 80% Efficiency. *Nat. Nanotechnol.* **2015**, *10* (4), 308−312.

(5) Wen, D.; Yue, F.; Li, G.; Zheng, G.; Chan, K.; Chen, S.; Chen, M.; Li, K. F.; Wong, P. W. H.; Cheah, K. W.; Yue Bun Pun, E.; Zhang, S.; Chen, X. Helicity Multiplexed Broadband Metasurface Holograms. *Nat. Commun.* **2015**, *6* (1), 8241.

(6) Hsu, W.-C.; Chang, C.-H.; Hong, Y.-H.; Kuo, H.-C.; Huang, Y.-W. Compact Structured Light Generation Based on Meta-Hologram PCSEL Integration. *Discover Nano* **2023**, *18* (1), 87.

(7) Yu, N.; Aieta, F.; Genevet, P.; Kats, M. A.; Gaburro, Z.; Capasso, F. A Broadband, Background-Free Quarter-Wave Plate Based on Plasmonic Metasurfaces. *Nano Lett.* **2012**, *12* (12), 6328−6333.

(8) Kats, M. A.; Genevet, P.; Aoust, G.; Yu, N.; Blanchard, R.; Aieta, F.; Gaburro, Z.; Capasso, F. Giant Birefringence in Optical Antenna Arrays with Widely Tailorable Optical Anisotropy. *Proc. Natl. Acad. Sci. U. S. A.* **2012**, *109* (31), 12364−12368.

(9) Chang, Y.-C.; Lin, C.-Y.; Su, H.-T.; Wu, Y.-C.; Hsu, C.-Y.; Chang, S.-M.; Huang, Y.-W. Directionally Asymmetric Holographic Imaging for Arbitrary Polarization States Using Janus Metasurfaces. *Adv. Opt. Mater.* **2025**, *13* (32), No. e01546.

(10) Lee, B.-R.; Chiang, M. F.; Ho, P. Y.; Chen, K.-H.; Lee, J.-H.; Hsu, P. H.; Peng, Y. C.; Hou, J.-Y.; Chen, S.-C.; Lee, Q.-Y.; Chang, C.-H.; Li, B.-R.; Lin, T.-E.; Lin, C.-T.; Shih, M.-H.; Lien, D.-H.; Lin, Y.-C.; Horng, R.-H.; Kivshar, Y.; Tseng, M. L. Deep-UV Silicon Polaritonic Metasurfaces for Enhancing Biomolecule Autofluorescence and Two-Dimensional Material Double-Resonance Raman Scattering. *Adv. Funct. Mater.* **2025**, *35* (14), 2420439.

(11) Shaltout, A. M.; Shalaev, V. M.; Brongersma, M. L. Spatiotemporal Light Control with Active Metasurfaces. *Science* **2019**, *364* (6441), No. eaat3100.

(12) Huang, Y.-W.; Xu, H.-X.; Sun, S.; Wu, Y.; Wang, Z.; Xiao, S.; Jiang, W. X.; Cui, T. J.; Tsai, D. P.; Qiu, C.-W. Structured Semiconductor Interfaces: Active Functionality on Light Manipulation. *Proc. IEEE* **2020**, *108* (5), 772−794.

(13) Sato, H.; Toda, K. Reflection-Type Electrically Controllable Diffraction Grating and Its Application to Intracavity Laser Modulation. *Appl. Opt.* **1977**, *16* (5), 1280−1288.

(14) A, K. R.; Ravindran, S. Investigating the Performance of a Novel Silicon Based P-i-n Modulator with Enhanced Carrier Injection. *Opt Quant Electron* **2024**, *56* (8), 1359.

(15) Huang, Y.-W.; Lee, H. W. H.; Sokhoyan, R.; Pala, R. A.; Thyagarajan, K.; Han, S.; Tsai, D. P.; Atwater, H. A. Gate-Tunable Conducting Oxide Metasurfaces. *Nano Lett.* **2016**, *16* (9), 5319−5325.

(16) Park, J.; Kang, J.-H.; Kim, S. J.; Liu, X.; Brongersma, M. L. Dynamic Reflection Phase and Polarization Control in Metasurfaces. *Nano Lett.* **2017**, *17* (1), 407−413.

(17) Shirmanesh, G. K.; Sokhoyan, R.; Wu, P. C.; Atwater, H. A. Electro-Optically Tunable Multifunctional Metasurfaces. *ACS Nano* **2020**, *14* (6), 6912−6920.

(18) Chung, H.; Miller, O. D. Tunable Metasurface Inverse Design for 80% Switching Efficiencies and 144° Angular Deflection. *ACS Photonics* **2020**, *7* (8), 2236−2243.

(19) Lewi, T.; Butakov, N. A.; Schuller, J. A. Thermal Tuning Capabilities of Semiconductor Metasurface Resonators. *Nanophotonics* **2018**, *8* (2), 331−338.

(20) Sun, M.; Xu, X.; Sun, X. W.; Liang, X.; Valuckas, V.; Zheng, Y.; Paniagua-Domínguez, R.; Kuznetsov, A. I. Efficient Visible Light Modulation Based on Electrically Tunable All Dielectric Metasurfaces Embedded in Thin-Layer Nematic Liquid Crystals. *Sci. Rep* **2019**, *9* (1), 8673.

(21) Hu, Y.; Ou, X.; Zeng, T.; Lai, J.; Zhang, J.; Li, X.; Luo, X.; Li, L.; Fan, F.; Duan, H. Electrically Tunable Multifunctional Polarization-Dependent Metasurfaces Integrated with Liquid Crystals in the Visible Region. *Nano Lett.* **2021**, *21* (11), 4554−4562.

(22) Rensberg, J.; Zhang, S.; Zhou, Y.; McLeod, A. S.; Schwarz, C.; Goldflam, M.; Liu, M.; Kerbusch, J.; Nawrodt, R.; Ramanathan, S.; Basov, D. N.; Capasso, F.; Ronning, C.; Kats, M. A. Active Optical Metasurfaces Based on Defect-Engineered Phase-Transition Materials. *Nano Lett.* **2016**, *16* (2), 1050−1055.

(23) Gutruf, P.; Zou, C.; Withayachumnankul, W.; Bhaskaran, M.; Sriram, S.; Fumeaux, C. Mechanically Tunable Dielectric Resonator Metasurfaces at Visible Frequencies. *ACS Nano* **2016**, *10* (1), 133−141.

(24) Ee, H.-S.; Agarwal, R. Tunable Metasurface and Flat Optical Zoom Lens on a Stretchable Substrate. *Nano Lett.* **2016**, *16* (4), 2818−2823.

(25) Lee, H. W.; Papadakis, G.; Burgos, S. P.; Chander, K.; Kriesch, A.; Pala, R.; Peschel, U.; Atwater, H. A. Nanoscale Conducting Oxide PlasMOStor. *Nano Lett.* **2014**, *14* (11), 6463−6468.

(26) Anopchenko, A.; Tao, L.; Arndt, C.; Lee, H. W. H. Field-Effect Tunable and Broadband Epsilon-Near-Zero Perfect Absorbers with Deep Subwavelength Thickness. *ACS Photonics* **2018**, *5* (7), 2631−2637.

(27) Sisler, J.; Thureja, P.; Grajower, M. Y.; Sokhoyan, R.; Huang, I.; Atwater, H. A. Electrically Tunable Space−Time Metasurfaces at Optical Frequencies. *Nat. Nanotechnol.* **2024**, *19* (10), 1491−1498.

(28) Jung, C.; Lee, E.; Rho, J. The Rise of Electrically Tunable Metasurfaces. *Sci. Adv.* **2024**, *10* (34), No. eado8964.

(29) Lee, Y.; Yun, J.; Kim, S.-J.; Seo, M.; In, S.; Jeong, H.-D.; Lee, S.-Y.; Park, N.; Chung, T. D.; Lee, B. High-Speed Transmission Control in Gate-Tunable Metasurfaces Using Hybrid Plasmonic Waveguide Mode. *Adv. Opt. Mater.* **2020**, *8* (22), 2001256.

(30) Forouzmand, A.; Salary, M. M.; Kafaie Shirmanesh, G.; Sokhoyan, R.; Atwater, H. A.; Mosallaei, H. Tunable All-Dielectric Metasurface for Phase Modulation of the Reflected and Transmitted Light via Permittivity Tuning of Indium Tin Oxide. *Nanophotonics* **2018**, *8* (3), 415−427.

(31) Thomaschewski, M.; Dong, C.; Gui, Y.; Wang, H.; Dalir, H.; Sorger, V. J. Free-Space Indium Tin Oxide Electro-Optic Transmission Modulator. *ACS Photonics* **2025**, *12* (1), 202−206.

(32) Benea-Chelmus, I.-C.; Mason, S.; Meretska, M. L.; Elder, D. L.; Kazakov, D.; Shams-Ansari, A.; Dalton, L. R.; Capasso, F. Gigahertz Free-Space Electro-Optic Modulators Based on Mie Resonances. *Nat. Commun.* **2022**, *13* (1), 3170.

(33) Dagli, S.; Shim, J.; Carr Delgado, H.; Balch, H. B.; Abdollahramezani, S.; Chen, C.-Y.; Dolia, V.; Klopfer, E.; Dixon, J.; Hu, J.; Ogunlade, B.; Song, J.-H.; Brongersma, M. L.; Barton, D.; Dionne, J. A. GHz-Speed Wavefront Shaping Metasurface Modulators Enabled by Resonant Electro-Optic Nanoantennas. *Adv. Mater.* **2025**, *37* (40), No. e06790.

(34) Soma, G.; Ariu, K.; Karakida, S.; Tsubai, Y.; Tanemura, T. Subvolt High-Speed Free-Space Modulator with Electro-Optic Metasurface. *Nat. Nanotechnol.* **2025**, *20* (11), 1625−1632.

(35) Thomaschewski, M.; Sokhoyan, R.; Schneider, E.; Atwater, H. Picometer-Scale Spatial Symmetry Breaking in Active Transmissive Metasurfaces. *arXiv* **2026**.

(36) Kim, J.; Sokhoyan, R.; Yi, M.; Han, S.; Atwater, H. A.; Jang, M. S. Overcoming Barriers to Dynamic Phase-Only Modulation in

Transmissive Metasurfaces via Diffraction Control. *ACS Nano* **2026**, *20* (8), 6622−6631.
(37) Zangeneh Kamali, K.; Xu, L.; Gagrani, N.; Tan, H. H.; Jagadish, C.; Miroshnichenko, A.; Neshev, D.; Rahmani, M. Electrically Programmable Solid-State Metasurfaces via Flash Localised Heating. *Light Sci. Appl.* **2023**, *12* (1), 40.
(38) Sokhoyan, R.; Hail, C. U.; Foley, M.; Grajower, M. Y.; Atwater, H. A. All-Dielectric High-Q Dynamically Tunable Transmissive Metasurfaces. *Laser Photonics Rev.* **2024**, *18* (6), 2300980.
(39) Gao, R.-Q.; Song, Q.; Liu, H.; Gao, J.-B.; Wang, X.-Y.; Bayanheshig; Li, C.; Ding, G.; Gong, Y.; Chen, X.-H.; Gao, J.-S. Design of Near-Infrared Reconfigurable Metalens on Silicon-On-Insulator (SOI) Platform with Fabry−Perrot Phase Shifter. *Opt. Commun.* **2019**, *446*, 56−63.
(40) Li, Z.; Pestourie, R.; Park, J.-S.; Huang, Y.-W.; Johnson, S. G.; Capasso, F. Inverse Design Enables Large-Scale High-Performance Meta-Optics Reshaping Virtual Reality. *Nat. Commun.* **2022**, *13* (1), 2409.
(41) Mansouree, M.; McClung, A.; Samudrala, S.; Arbabi, A. Large-Scale Parametrized Metasurface Design Using Adjoint Optimization. *ACS Photonics* **2021**, *8* (2), 455−463.
(42) Tsai, W.-C.; Yang, P.-C.; Yen, A.-R.; Wu, Y.-C.; Huang, Y.-W. Twisted Light Beam From a Gradient-Based Inverse-Designed Metasurface. *J. Lightwave Technol.* **2025**, *43* (23), 10584−10590.
(43) Sell, D.; Yang, J.; Doshay, S.; Yang, R.; Fan, J. A. Large-Angle, Multifunctional Metagratings Based on Freeform Multimode Geometries. *Nano Lett.* **2017**, *17* (6), 3752−3757.
(44) Su, H.-T.; Wang, L.-Y.; Hsu, C.-Y.; Wu, Y.-C.; Lin, C.-Y.; Chang, S.-M.; Huang, Y.-W. Topology Optimization Enables High-Q Metasurface for Color Selectivity. *Nano Lett.* **2024**, *24* (33), 10055−10061.
(45) Liu, Y.-T.; Wu, Y.-C.; Lin, C.-Y.; Su, H.-T.; Zhou, Y.-Q.; Huang, Y.-W. Topology Optimization Enables Freeform Matrix Fourier Optics. *Adv. Opt. Mater.* **2025**, *13* (24), 2500872.
(46) Hsu, C.-Y.; Su, H.-T.; Kuo, W.-T.; Li, W.-Z.; Liu, Y.-T.; Chang, Y.-C.; Huang, Y.-W. Two-Dimensional Topology Optimized Nonlocal Metasurfaces for Augmented Reality. *Nano Lett.* **2026**, *26*, 4080−4088.
(47) Lin, C.-H.; Chen, Y.-S.; Lin, J.-T.; Wu, H. C.; Kuo, H.-T.; Lin, C.-F.; Chen, P.; Wu, P. C. Automatic Inverse Design of High-Performance Beam-Steering Metasurfaces via Genetic-Type Tree Optimization. *Nano Lett.* **2021**, *21* (12), 4981−4989.
(48) Hsu, W.-L.; Yu, C.-Y.; Huang, Y.-S.; Zeng, Q.-C.; Chen, Y.-C.; Lu, G.-H.; Weng, C.-J.; Chen, F.-Z.; Chen, C.-C.; Wang, C.-M. Simplest but Efficient Design of a Color Router Optimized by Genetic Algorithms. *ACS Photonics* **2025**, *12* (3), 1402−1408.
(49) Liu, Z.; Zhu, D.; Rodrigues, S. P.; Lee, K.-T.; Cai, W. Generative Model for the Inverse Design of Metasurfaces. *Nano Lett.* **2018**, *18* (10), 6570−6576.
(50) Ma, W.; Liu, Z.; Kudyshev, Z. A.; Boltasseva, A.; Cai, W.; Liu, Y. Deep Learning for the Design of Photonic Structures. *Nat. Photonics* **2021**, *15* (2), 77−90.
(51) Thureja, P.; Shirmanesh, G. K.; Fountaine, K. T.; Sokhoyan, R.; Grajower, M.; Atwater, H. A. Array-Level Inverse Design of Beam Steering Active Metasurfaces. *ACS Nano* **2020**, *14* (11), 15042−15055.
(52) Park, J.; Jeong, B. G.; Kim, S. I.; Lee, D.; Kim, J.; Shin, C.; Lee, C. B.; Otsuka, T.; Kyoung, J.; Kim, S.; Yang, K.-Y.; Park, Y.-Y.; Lee, J.; Hwang, I.; Jang, J.; Song, S. H.; Brongersma, M. L.; Ha, K.; Hwang, S.-W.; Choo, H.; Choi, B. L. All-Solid-State Spatial Light Modulator with Independent Phase and Amplitude Control for Three-Dimensional LiDAR Applications. *Nat. Nanotechnol.* **2021**, *16* (1), 69−76.

https://doi.org/10.1021/acsanm.6c01415
ACS Appl. Nano Mater. 2026, 9, 14707−14717